Research Article

Abdulrahman I. Alateyah, Adel M. A. Mohamed, Waleed H. El-Garaihy*, Majed Alinizzi, Mansour Alturki, Mohamed S. El-Asfoury, Eman M. Zayed, and Hussein Zein

Tailoring ZX30 alloy's microstructural evolution, electrochemical and mechanical behavior *via* ECAP processing parameters

https://doi.org/10.1515/rams-2025-0149
received February 14, 2025; accepted August 18, 2025

Abstract: This study investigates the effect of equal channel angular pressing (ECAP) parameters, specifically die angle and no. of passes, on the microstructural, electrochemical, and mechanical properties of biodegradable ZX30 magnesium alloy. The alloy was processed using ECAP at die angles of 90° and 120° with one and four passes *via* route Bc, resulting in substantial microstructural refinement and texture modification. Compared to the as-annealed (AA) condition, four ECAP passes at 90° and 120° die angles reduced the grain size dramatically by 91.6% (to 2.2 μm) and 92.7% (to 1.9 μm), respectively. The processing parameters promoted dynamic recrystallization and increased high-angle grain boundary density, enhancing both corrosion resistance and mechanical strength. Electrochemical impedance spectroscopy and potentiodynamic polarization tests confirmed a corrosion rate reduction of up to 93% with the 4Bc-90° die angle, attributed to grain refinement and increased charge transfer resistance. Grain boundaries act as barriers to corrosion by limiting dislocation movement and reducing electrochemical reactivity at the grain surface, as further supported by 15-day immersion tests. Mechanical testing showed notable improvement, with hardness and tensile strength increasing by up to 66 and 56%, respectively, under optimal ECAP conditions (4Bc-120° die) compared to the AA. These findings highlight the critical role of ECAP parameters – particularly die angle and number of passes – in tailoring of ZX30 alloy properties and underscore ECAP's efficacy as a non-chemical, parameter-controlled strategy for enhancing microstructure, corrosion resistance, and mechanical performance in ZX30 magnesium alloys for construction and biomedical applications.

Keywords: mechanical properties, electrochemical behavior, microstructure, texture analysis

*** Corresponding author: Waleed H. El-Garaihy**, Department of Mechanical Engineering, College of Engineering, Qassim University, Buraydah, 51452, Saudi Arabia, e-mail: w.nasr@qu.edu.sa
Abdulrahman I. Alateyah: Department of Mechanical Engineering, College of Engineering, Qassim University, Buraydah, 51452, Saudi Arabia, e-mail: a.alateyah@qu.edu.sa
Adel M. A. Mohamed: Metallurgical and Materials Engineering Department, Faculty of Petroleum and Mining Engineering, Suez University, Suez, 43512, Egypt, e-mail: adel.mohamed25@yahoo.com
Majed Alinizzi: Department of Civil Engineering, College of Engineering, Qassim University, Buraydah, 51452, Saudi Arabia, e-mail: Alinizzi@qu.edu.sa
Mansour Alturki: Department of Civil Engineering, College of Engineering, Qassim University, Buraydah, 51452, Saudi Arabia, e-mail: m.alturki@qu.edu.sa
Mohamed S. El-Asfoury: Production Engineering and Mechanical Design Department, Faculty of Engineering, Port-Said University, Port-Said, 42523, Egypt, e-mail: mohamed.saad@eng.psu.edu.eg
Eman M. Zayed: Mechanical Engineering Department, Faculty of Engineering, The British University in Egypt (BUE), El-Sheroukcity, Cairo, 11837, Egypt, e-mail: eman.zayed@bue.edu.eg
Hussein Zein: Department of Mechanical Engineering, College of Engineering, Qassim University, Buraydah, 51452, Saudi Arabia; Mechanical Design and Production Department, Faculty of Engineering, Cairo University, Giza, 12613, Egypt, e-mail: H.Hussein@qu.edu.sa

1 Introduction

Magnesium (Mg) and its alloys are increasingly recognized as essential materials for structural and biomedical engineering due to their lightweight nature, high specific strength, and superior machinability [1–3]. These characteristics position Mg alloys as a transformative alternative in automotive, construction, and aerospace industries, where weight reduction significantly enhances performance and efficiency. However, challenges such as limited strength, ductility, and corrosion resistance remain barriers to widespread application [4–6]. Recent advancements have addressed these issues by enhancing mechanical properties and improving durability [7,8]. These improvements align with the rising interest in Mg as a sustainable substitute for heavier materials like steel and aluminum, providing significant energy savings and reductions in carbon emissions. The ongoing research highlights the material's potential and ignites further

investigations, signaling a pivotal shift in its adoption for structural and biomedical engineering.

To tackle the uncontrolled degradation of Mg alloys, various approaches, including the development of novel alloys, composites, and protective coatings, have been extensively studied [9–12]. Experiments have explored alloying Mg with elements such as Zn, Zr, Ca, Li, Al, Mn, Sr, or Si, or even rare earth (RE) elements like Ce, La, Nd, Pr, Y, Gd, or Sc, enhancing both biocompatibility and mechanical and corrosion resistance [13–15]. Nevertheless, alloying Mg is challenging due to its high chemical reactivity and propensity for oxidation and evaporation. Among these alloys, the Mg-ZX system (Mg–Zn–Ca) has emerged as biocompatible, economical, and easy to produce, making it particularly appealing [16]. Specifically, Zn significantly contributes to solid-solution strengthening and improved corrosion resistance [17–19]. Further, Ca is one of the most essential chemical components in human bones, and it promotes the creation of hydroxyapatite in the body, hence accelerating bone repair [20,21]. The equilibrium limit of Zn and Ca solubility in Mg is 6.2 wt% at 340 C, and 1.11 wt% at 521 C, respectively [22]. However, reliance solely on alloying elements can cause undesirable segregations, impure inclusions, and second-phase formations. Therefore, deformation processing techniques have been employed to control such structural irregularities, including second-phase distribution, substructure refinement, micro-strains, textures, and intentional grain size modification [23].

Enhancing corrosion resistance in Mg alloys through mechanical methods, particularly microstructural modification, has recently received widespread attention [24–26]. Due to the substantial role grain boundaries play in biodegradation within physiological environments, grain size has become a crucial determinant for biodegradable Mg-based materials [27]. Grain boundaries and grain interiors differ significantly in atomic reactivity, diffusion rates, and atomic coordination. Thus, grain refinement achieved through deformation processes has become a promising strategy for improving Mg alloys' strength, ductility, and corrosion resistance. For ZX alloys, understanding the grain size evolution during deformation is vital for enhancing these properties [28–30]. In this context, severe plastic deformation (SPD) processes such as equal channel angular pressing (ECAP), high pressure torsion (HPT), and accumulative roll bonding (ARB) have demonstrated their ability in creating sub-micron ultrafine-grained microstructure in numerous Mg-based alloys [31–34]. For instance, ZX alloys processed by HPT demonstrate grain refinement, significant fragmentation, and uniform secondary-phase dispersion, altering corrosion modes from localized pitting to uniform corrosion [35]. Chen *et al.* [36] found that high strain rate rolling refined Mg alloys better than traditional rolling, improving corrosion resistance. The AZ91 alloy's corrosion rate increased due to the accumulation of a high dislocation density and the transformation of the phase's morphology from a continuous net shape into isolated particles [37,38]. Ralston *et al.* [39] used a Hall-Petch equation to relate grain size to corrosion rate. Numerous studies employed this equation to describe the corrosion behavior that altered following grain refinement by plastic deformation [40,41].

Hence, improvements in mechanical and corrosion performance of Mg alloys processed *via* ECAP are primarily attributed to grain refinement, as described by the Hall-Petch equation. However, factors like crystallographic texture significantly influence material properties, notably affecting the strength coefficient (*K*-value). Among ECAP parameters, processing routes (particularly route Bc) and temperature critically determine grain refinement and mechanical properties [42]. Lower processing temperatures often require more ECAP passes to develop homogeneous, equiaxed microstructures, improving both ductility and strength. For instance, at 220°C, after 8 passes, a heterogeneous microstructure maintained a favorable balance between strength and ductility, attributed not only to grain size but also to texture evolution [43,44]. Furthermore, high-angle grain boundaries (HAGBs) and low-angle grain boundaries (LAGBs) play a key role in this transformation. During ECAP, the proportion of HAGBs increases while that of LAGBs decreases, resulting in refined microstructures that enhance mechanical properties and isotropy. For example, pure Mg processed by 7 ECAP passes exhibited ultra-fine grains as the HAGB fraction increased, while LAGBs and twin boundaries became more prevalent [45]. An 80% HAGB fraction was observed in AX41 Mg alloy after 8 passes, both in as cast and extruded conditions [43]. Exploring the relationship between grain size, crystallographic orientation, and the formation of protective surfaces is essential for understanding applications in corrosive environments. Typically, grain refinement promotes the formation of a more robust passive film, improving corrosion resistance. For instance, finer grains in pure Mg were shown to reduce the corrosion rate in NaCl solution [46]. However, texture evolution combined with grain refinement significantly influences corrosion resistance by promoting protective passive films, although certain defects introduced during ECAP may enhance corrosion under specific conditions [47,48]. Thus, optimizing grain structure and crystallographic texture through ECAP is essential for achieving optimal mechanical and corrosion properties.

This work clarifies the correlation between corrosion rate and grain size by emphasizing the influence of ECAP parameters such as die angle, processing route and number of passes, while isolating other variables such as deformation temperature, die geometry, and alloying composition. As seen in Figure 1, the Mg-3wt%Zn-0.4 wt%Ca (ZX30) alloy was processed using ECAP with die angles of 90° and 120° under multiple passes. The resulting microstructure, texture evolution, and mechanical performance were systematically investigated. Electrochemical polarization and impedance spectroscopy analyses were conducted to evaluate corrosion behavior. This non-chemical approach offers precise control over corrosion characteristics, optimizing the ZX30 alloy's degradation behavior and mechanical performance, thereby enhancing its suitability in structural and biomedical contexts.

2 Materials and methods

The ZX30 alloy, with a nominal composition of Mg-3 wt% Zn-0.4 wt% Ca, was procured for this study. Before processing, the as-received material was machined to fit the die entrance channel (14 mm diameter) and annealed at 430°C for 16 h prior to extrusion (AA). Extrusion was performed using ECAP dies with channel angles of 90° and 120°, at a temperature of 250°C and at a speed of 10 mm·min^{-1}. The ECAP process involved one and four passes following route Bc (1P, 4Bc) for both die angles. ECAPed samples were produced in the shape of a rod with a diameter of 14 mm and the length of about 60 mm, the homogenized central portion was used for further characterization.

Microstructure analysis was carried out using a scanning electron microscope (SEM, SU-70) equipped with an electron backscatter diffraction (EBSD) system. EBSD scans were conducted at 100 nm intervals from the ED plane, with data analyzed using Channel 5 software. For SEM specimen preparation, the samples underwent grinding with SiC abrasive papers, followed by polishing with diamond paste and etching with an Acetic-Picral solution. For EBSD specimen preparation, electrolytic polishing replaced the etching step. X-ray diffraction (XRD, JEOL JDX-8030) was conducted at room temperature in the 2θ range from 20° to 80° with a step size of 0.02°, using Cu/Ka radiation (40 kV, 30 mA). Additionally, Energy-dispersive X-ray spectroscopy (EDS) was employed to determine the elemental composition.

Corrosion analysis was conducted using a dynamic potential polarization test with an SP-200 Potentiostat (Bio-Logic, Orlando, FL, USA). A three-electrode system was employed, where the sample, with a fixed exposed area of 6 cm^2, served as the working electrode, a platinum sheet was used as the counter electrode, and a saturated calomel electrode acted as the reference electrode. Ringer lactate solution, maintained at 37 ± 0.5°C, was used as the electrolyte. Before the measurements, the open circuit potential was allowed to stabilize to ensure dynamic equilibrium between the sample and the electrolyte. The dynamic potential scan was then performed, with a voltage range of 250 mV and a scanning rate of 0.166 mV·s^{-1}. The electrochemical impedance spectroscopy (EIS) was carried out over frequencies ranging from 100 Hz to 1 MHz, with a potential window of ±10 mV. Additionally, a weight loss experiment was conducted on samples measuring 14 mm in diameter and 5 mm in thickness. The samples were

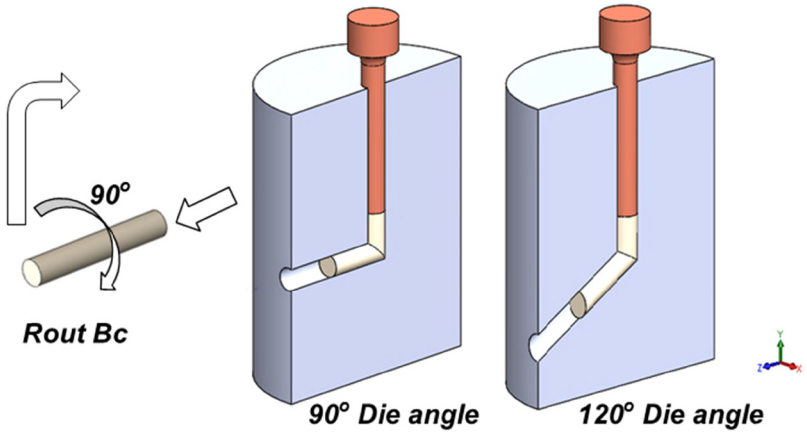

Figure 1: Schematic Cad drawing of the ECAP process, showing die angles of 90° and 120° using Route Bc. In Route Bc, the billet is rotated by 90° in the same direction between consecutive passes.

cleaned and polished to prevent surface contamination before immersion in Ringer lactate for up to 360 h at 37°C, simulating human body temperature. The samples were periodically cleaned to remove corrosion products and weighed at regular intervals to measure the corrosion progress.

Tensile and hardness tests were employed to evaluate the mechanical properties. The tensile tests were carried out using a computerized universal testing machine at a strain rate of 10^{-3} s^{-1} and room temperature. To ensure reliable results, at least three samples were tested for each alloy condition. Cylindrical tensile specimens were prepared with the loading applied along the extrusion direction (ED). Vickers microhardness measurements were conducted using an automatic microhardness tester (Qualitest, Canada) with a 0.5 kg load and a dwell time of 15 s. The microhardness indentations, approximately 20 µm in size, were evaluated at ten different points for each sample.

3 Results and discussion

3.1 Energy-dispersive spectroscopy elemental map

The microstructures of the ZX30 alloy after annealing for 16 h at 430°C, along with elemental mapping and EDS spectrum analysis, are shown in Figure 2. The SEM analysis

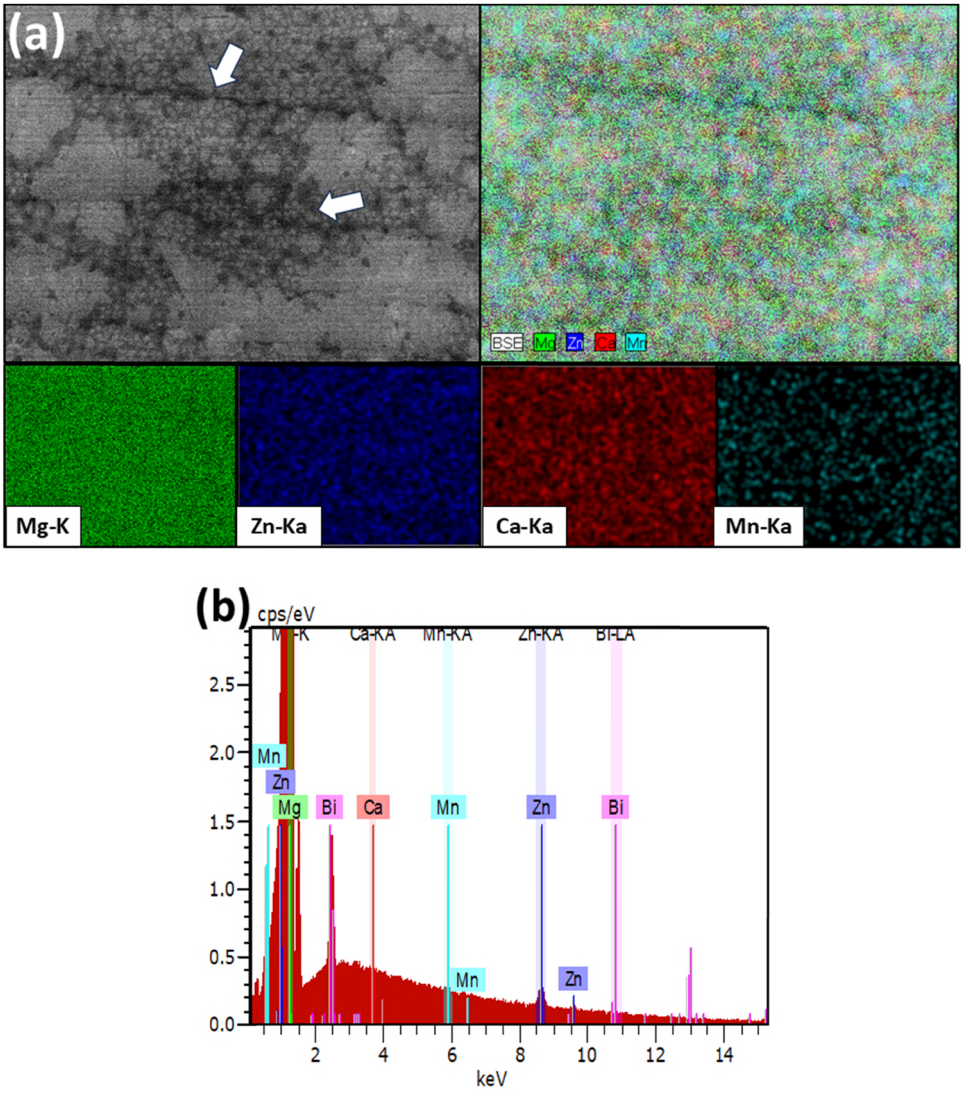

Figure 2: The SEM imaging and EDS elemental analysis of the AA-ZX30 alloy: (a) the SEM microstructure and elemental mapping (5k magnification) and (b) the corresponding EDS spectrum analysis.

revealed that the alloy primarily consists of equiaxed grains, with noticeable grain coarsening due to the annealing process (indicated by white arrows in Figure 2). Principally, fine grain nucleation occurs predominantly along grain and twin boundaries due to increased stress, which activates harder slip systems [49]. Hence, smaller grain sizes, in turn, promote non-basal slip and dynamic recrystallization, aiding in fine grain formation, as discussed in subsequent sections. EDS analysis confirmed the presence of Mg, Zn, Ca, and Mn, uniformly distributed throughout the grain structure. Previous studies indicate that primary phases typically include α-Mg and fine globular precipitated phase Ca_2Mg6Zn_3, as further verified by XRD analysis [50].

3.2 Grain structure and crystallographic texture

Figure 3 gives details on the microstructural characteristics of the as-annealed (AA) condition of ZX30 alloy, by showing

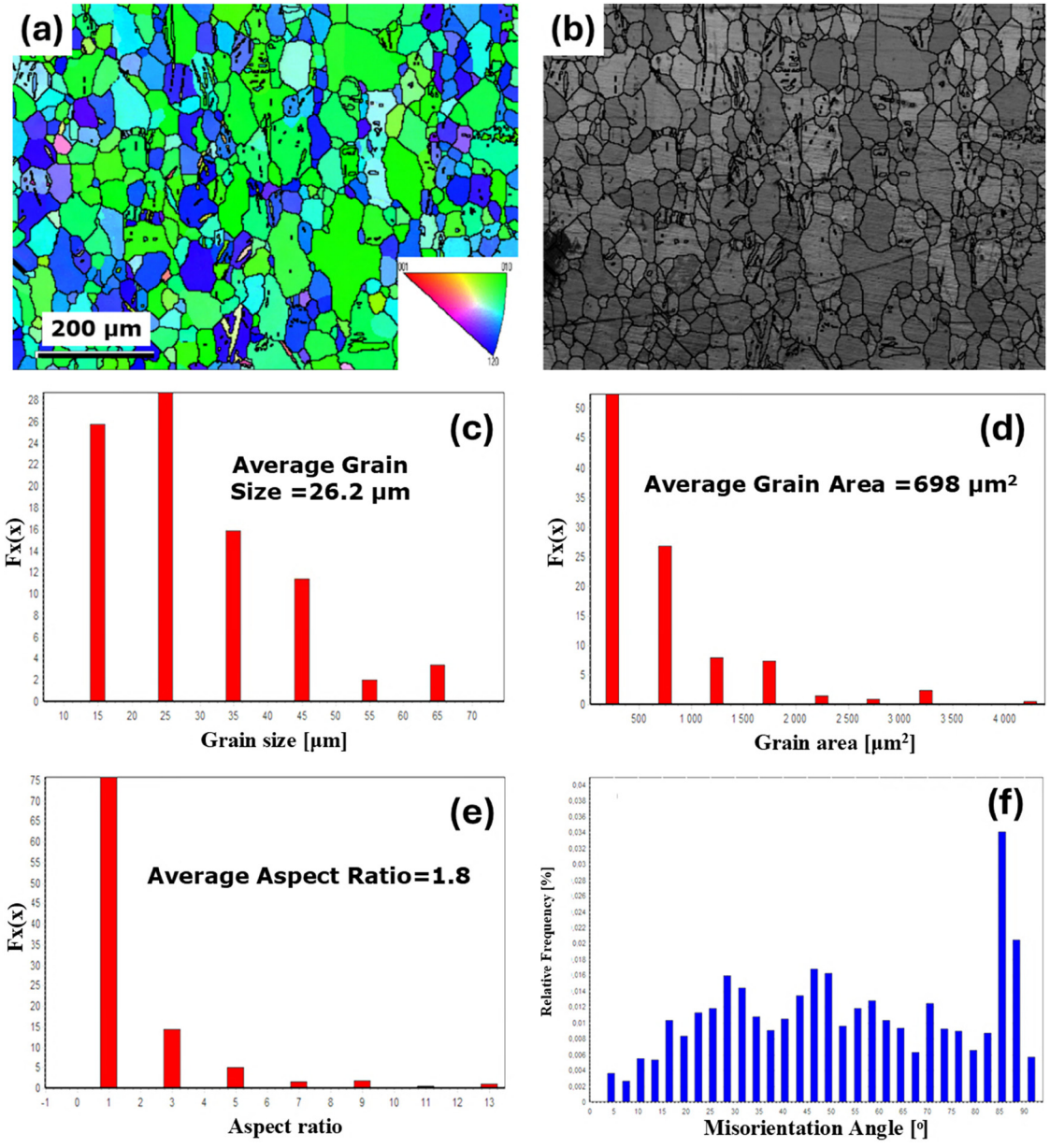

Figure 3: AA ZX30's (a) colored IPF map relative to ED, (b) its corresponding band contrast map, (c) grain size distribution, (d) grain area distribution, (e) grain aspect ratio distribution, and (f) misorientation angle distribution.

several key structural parameters. The inverse pole figure (IPF) map relative to ED shown in Figure 3a provides grain orientations of the alloy. A further band contrast map, shown in Figure 3b, highlights grain boundaries and internal features of the alloy to assist the visualization of grain structure. Figure 3c presents the grain size distribution, showing an average diameter of 26.2 µm, whereas Figure 3d presents the distribution of the grain area with an average value of 698 μm^2. In Figure 3e, the distribution of the aspect ratio of the grains is presented; this shows an average value of 1.8 and points toward the main characteristics of partially equiaxed grain structure with light grain elongation. Figure 3f shows the distribution of misorientation angle, which indicates the angular relation between adjacent grains. Hence, the AA sample reveals a characteristic annealed microstructure, featuring isolated recrystallization twins and a dominant presence of HAGBs, indicative of thorough recrystallization. Notably, certain regions exhibit irregular grain growth, deviating from typical uniformity, which may have a significant effect on mechanical properties and corrosion behavior [42].

Figures 4 and 5 show the microstructural evolution of ZX30 alloy processed by ECAP at different die angles and number of passes. In Figure 4, IPF maps and band contrast maps present the microstructure after one pass (1P) and after four passes *via* route Bc (4Bc) using a 90° die angle; high angle bands (HABs) are depicted in black and low angle band (LABs) in red. Comparable analyses for the ZX30 alloy processed with a 120° die under identical conditions are shown in Figure 5. It is evident that increasing the number of passes results in a marked reduction in grain size, corresponding to greater strain accumulation and enhanced grain boundary formation.

Figures 6 and 7 provide a more detailed analysis of the grain size, grain area, grain aspect ratio, and misorientation angle distributions of ZX30 alloy samples processed through ECAP for different die angles (90° and 120°) and passes (1P and 4Bc). These parameters clarify the critical role of ECAP in achieving significant refinement and homogeneity, both significant keys toward the improvement of alloys' performance. Compared to the AA condition, the ECAP-processed samples exhibit a dramatic reduction in grain size. In the 1P-90° condition, the grain size was reduced to 3.5 µm, marking an 86.6% reduction from the original AA structure. Further processing to the 4Bc-90° condition decreased the grain size to 2.2 µm, achieving a 91.6% reduction. For the 120° die, grain size refinement was slightly less pronounced; the 1P-120° condition reached 3.85 µm, while 4Bc_120° achieved 1.9 µm, a 92.7% reduction. These substantial reductions demonstrate the effectiveness of ECAP processing parameters for microstructural refinement, with four passes notably enhancing dynamic recrystallization (DRX) and increasing the density of ultrafine

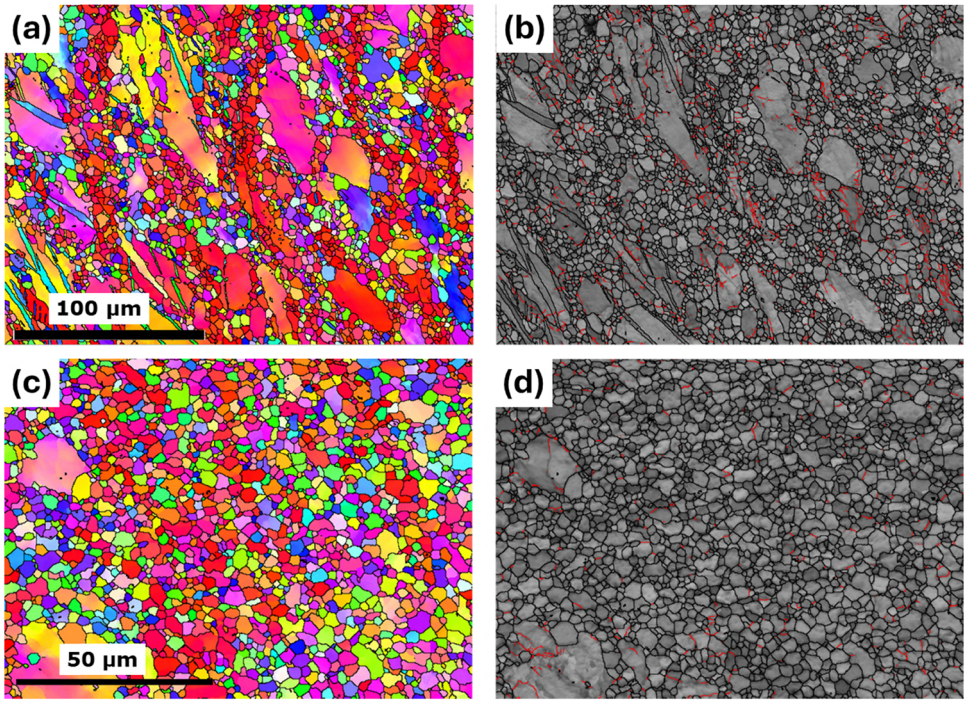

Figure 4: Colored IPF maps and their corresponding band contrast maps with HABs (Black lines) and LABs (Red lines) superimposed for an ECAP processed Mg alloy ZX30 after (a) and (b) 1P_ 90° die, and (c) and (d) 4Bc_90° die.

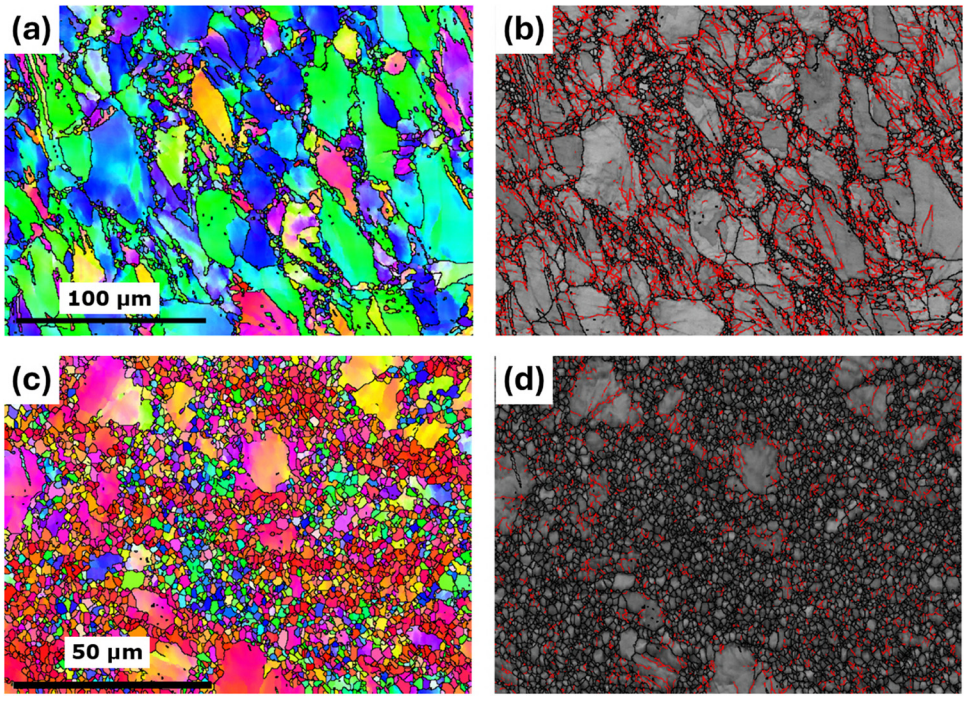

Figure 5: Colored IPF maps and their corresponding band contrast maps with HABs (Black lines) and LABs (Red lines) superimposed for an ECAP processed Mg alloy ZX30 after (a) and (b) 1P_ 120° die, and (c) and (d) 4Bc_120° die.

equiaxed grains, as seen in Figures 4d and 6d. The statistical data of the grain size of ZX30 are displayed in Table 1.

ECAP processing significantly reduces the average grain area. For a 90° die, 1P yields an average grain area of 14.5 μm^2 (97.9% reduction), further decreasing to 5.3 μm^2 after four passes (99.2% reduction). With a 120° die, one pass results in a 20.4 μm^2 area (97.1% reduction), and 4Bc further reduce it to 3.9 μm^2 (99.4% reduction). These findings reinforce that both die angles can induce a pronounced decrease in grain areas, with the most substantial effect observed after multiple passes. Notably, the 90° die consistently produced smaller grain areas, indicating that sharper angles are more favorable for achieving finer grains.

Regarding the average aspect ratio, after 1P with the 90° die, decreases to 1.7, while 4Bc decreases the ratio further to 1.4, which accounts for a 22.2% decrease. In the case of the 120° die, after 1P, the ratio was 1.85 (a slight increase of 2.8% compared with AA), but with 4Bc, it decreases to 1.65, an 8.3% reduction from AA. These findings confirm that ECAP processing not only refines grain size but also produces more equiaxed grains, especially in multi-pass conditions and with a 90° die.

The misorientation angle distributions in both die angles, as depicted in Figures 6g, h and 7g, h illustrate an increase in the proportion of HAGBs with additional passes, which generally suggests increased integrity of the boundaries and possibly enhancement of mechanical strength. The microstructural evolution from the large, heterogeneous grains in the AA condition to a highly refined and equiaxed structure with increased HAGBs in the 4Bc conditions assesses that die angle and number of passes are very important for achieving the finest and homogeneous structure, which can be expected to confer superior corrosion resistance and mechanical stability [51]. The observed increase in HAGB density with multiple ECAP passes can be attributed to the conversion of LAGBs to HAGBs during recrystallization.

The crystallographic texture analysis of the ZX30 alloy, as represented by the pole figures of the {0001}, {11-20}, and {10-10} planes (Figure 8), indicates remarkable differences between the AA condition and the specimens processed by ECAP. For ZX30, in the AA condition, a strong texture is present, with the maximum intensity of all analyzed planes amounting to 10.7 times random (Figure 8a). This is accompanied by a sharp {0001} fiber texture oriented perpendicular to the ED, while the {11-20} and {10-10} planes are nearly parallel to the ED – characteristics indicative of a well-defined crystallographic alignment in the AA sample.

Following ECAP processing, the texture intensity changes depending on both the number of passes and the die angle, demonstrating the influence of these parameters on grain orientation. For the 1P_90° condition (Figure 8b), the texture intensity slightly increases to 11.2 times random between the planes {0001}, {11-20}, and {10-10}; suggesting that one pass at

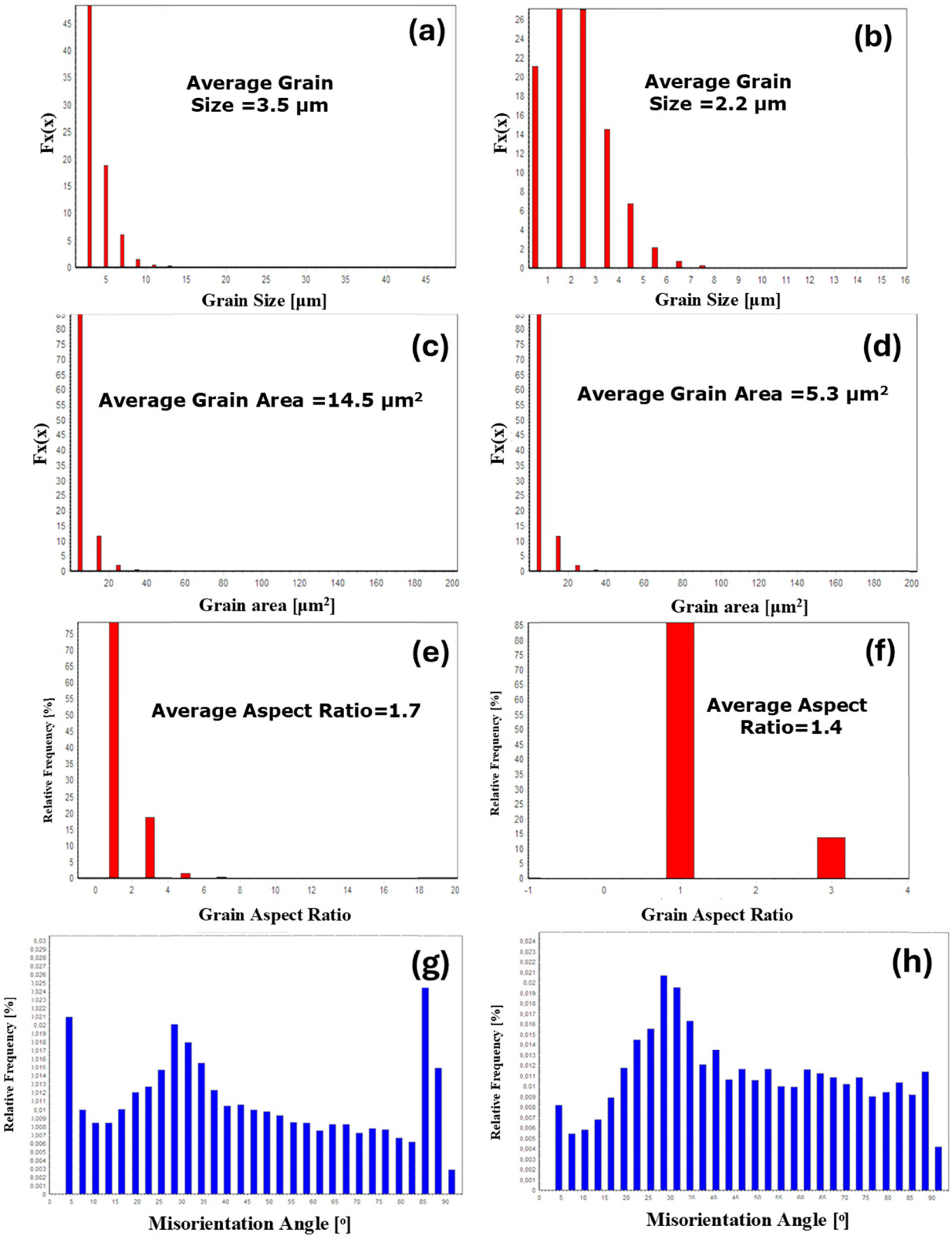

Figure 6: (a) and (b) grain size distribution, (c) and (d) grain area distribution, (e) and (f) grain aspect ratio distribution, and (g) and (h) misorientation angle distribution of ZX30 alloy processed through (a), (c), (e), and (g) 1P_90° die and (b), (d), (f), and (h) 4Bc_90° die.

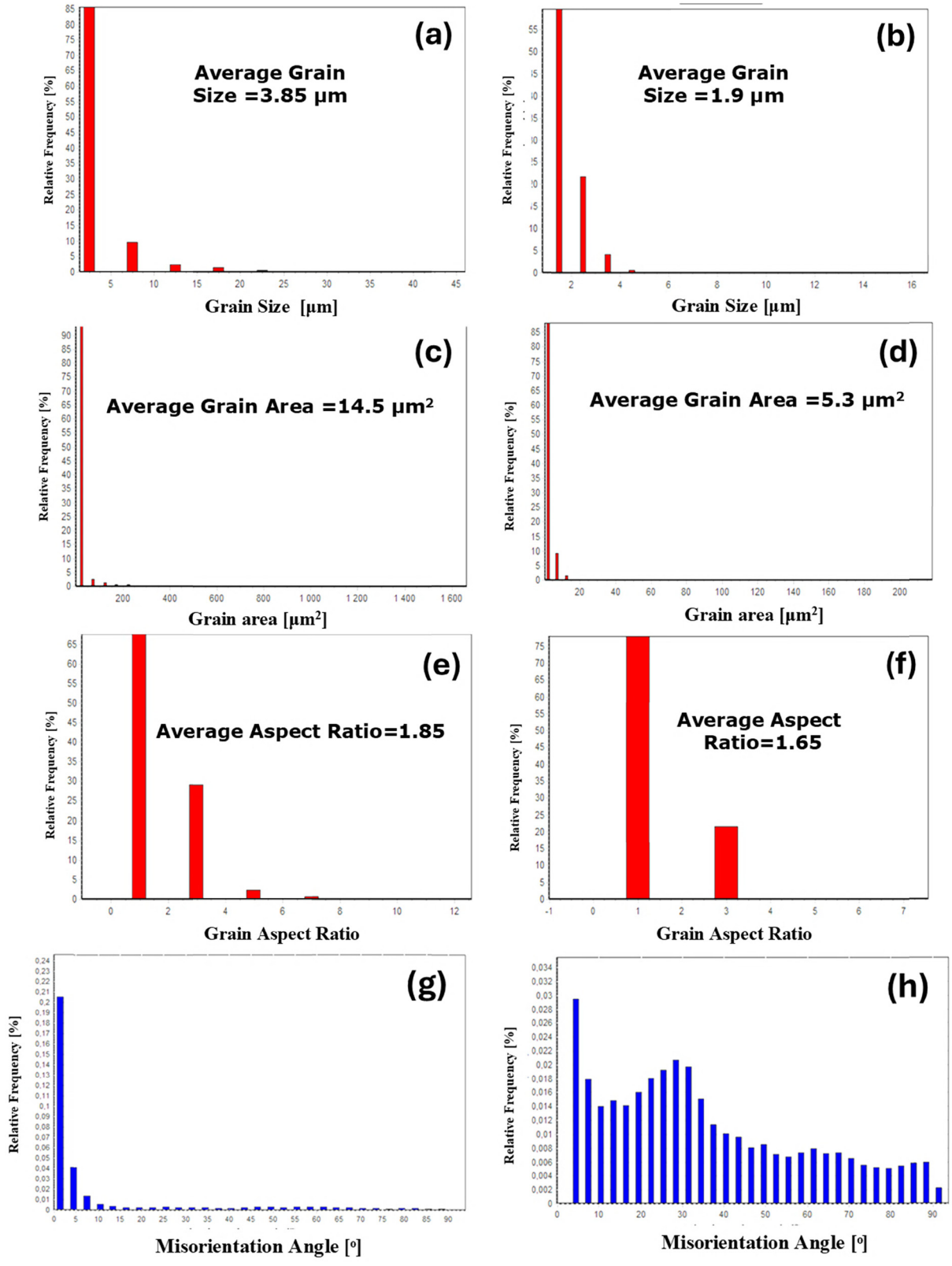

Figure 7: (a) and (b) grain size distribution, (c) and (d) grain area distribution, (e) and (f) grain aspect ratio distribution, and (g) and (h) misorientation angle distribution of ZX30 alloy processed through (a), (c), (e), and (g) 1P_ 120° die and (b), (d), (f), and (h) 4Bc_120° die.

Table 1: Statistical data of grain size of AA and ECAPed ZX30 alloy billets

Item	AA	1P_90°	4Bc_90°	1P_120°	4Bc_120°
Average grain size (EX)	26.2	3.5	2.2	3.85	1.9
Standard deviation (s)	14.29	2.4981	1.4009	3.5708	0.85012
Coefficient of variation (s/EX)	0.5456	0.71299	0.64065	1.0335	0.49248
Minimum value (Xmin)	7.0467	1.1848	0.22568	1.382	0.81369
Maximum value (Xmax)	74.712	48.705	16.05	46.012	16.666

90° die angle causes a reasonable strengthening of the crystallographic alignment. On the contrary, the 4Bc_90° condition shows a maximum intensity reduction to 10.1 times random (Figure 8c). That indicates that after several passes with the 90° die, the initial alignment is partly relaxed. This effect could be explained due to the fact that with each additional pass, the grains are being rearranged into a more refined yet less textured structure.

Conversely, the 120° die angle promotes a much more pronounced crystallographic alignment, as shown in Figure 8d and e. The intensity of texture for the 1P-120° condition reaches 14.25 times random, indicating increased alignment significantly influenced by the action of the increased die angle on grain flow. This improved texture is principally because of the higher shear imposed by the 120° die angle, which increases alignment along with the ED. For the case of the 4Bc-120°, the texture drops to 11.85 times random. This decrease with increased passes, like the observation in the 90° die, shows that multiple passes tend to relax an initially high alignment by allowing more grain reorientation and spreading within the structure.

Thus, AA-ZX30 alloy initially exhibits a uniform distribution of the course equiaxed grains. After four passes of ECAP, these large grains are fragmented into numerous substructures, accompanied by a pronounced increase in dynamic recrystallization evidenced by the formation of finer grains and greater HAGBs. Grain sizes refine to 2.2 and 1.9 μm using die angles of 90° and 120°, respectively. These differences in refinement arise from the variation in strain intensity imparted by the die angle; sharper angles yield higher shear strain, promoting effective recrystallization. While the 120° die angle slows refinement due to reduced strain, it still affects the microstructure due to deformation mechanisms. After one pass, distinct grain orientations, categorized by color, reflect the influence of die angle. This mixed grain morphology highlights the processing conditions' impact, particularly how dynamic recrystallization occurs primarily along twin boundaries and coarse grain boundaries [52,53]. The interplay between activated slip systems and shear stresses at grain boundaries further facilitates new grain nucleation, confirming that efficient grain refinement in hexagonally close-packed structures relies on activating multiple slip systems and increasing boundary stresses [54]. Additionally, mechanisms like particle stimulated nucleation and the pinning effect of fine particles hinder the growth of dynamically recrystallized grains, contributing to the observed refinement in the 120° die angle and forming a strong fiber texture [55]. These results show that die angle and the number of passes are the two most critical variables in controlling the crystallographic texture in ZX30 alloy and that a die angle of 120° is effective for improving crystallographic alignment. Hence, any modification of these variables could have quite significant repercussions on material properties, especially anisotropic ones, and any mechanical performance relevant to applications.

3.3 XRD

The XRD analysis of the AA and ECAP-processed ZX30 alloy samples, as shown in Figure 9a, reveals key insights into the microstructural evolution of the alloy. The diffraction peaks are predominantly indexed to the α-Mg phase, confirming that the matrix incorporates Zn and Ca in proportions consistent with the alloy's composition. No signs of oxidation or formation of new crystalline phases due to the extrusion process were detected. It is well known that alloying elements or impurities pin dislocations, hindering their movement and annihilation during SPD, which influences microstructural development during ECAP [42].

The extruded samples exhibit a strong texture orientation and a limited presence of secondary phases. Based on XRD and EDS analysis, the secondary phase, $Ca_2Mg_6Zn_3$, constitutes approximately 3.5% of the alloy's volume, reflecting the high Zn/Ca ratio [56]. In the AA condition, the intensity of this phase increases at specific angles (~32°, 36°, 41°, and 43°), while after the ECAP process, the secondary phases become more dispersed and dissolve within the Mg matrix, resulting in a notable decrease in their intensity. This reduction is likely due to the thermoplastic deformation induced by ECAP. Also, a slight angular

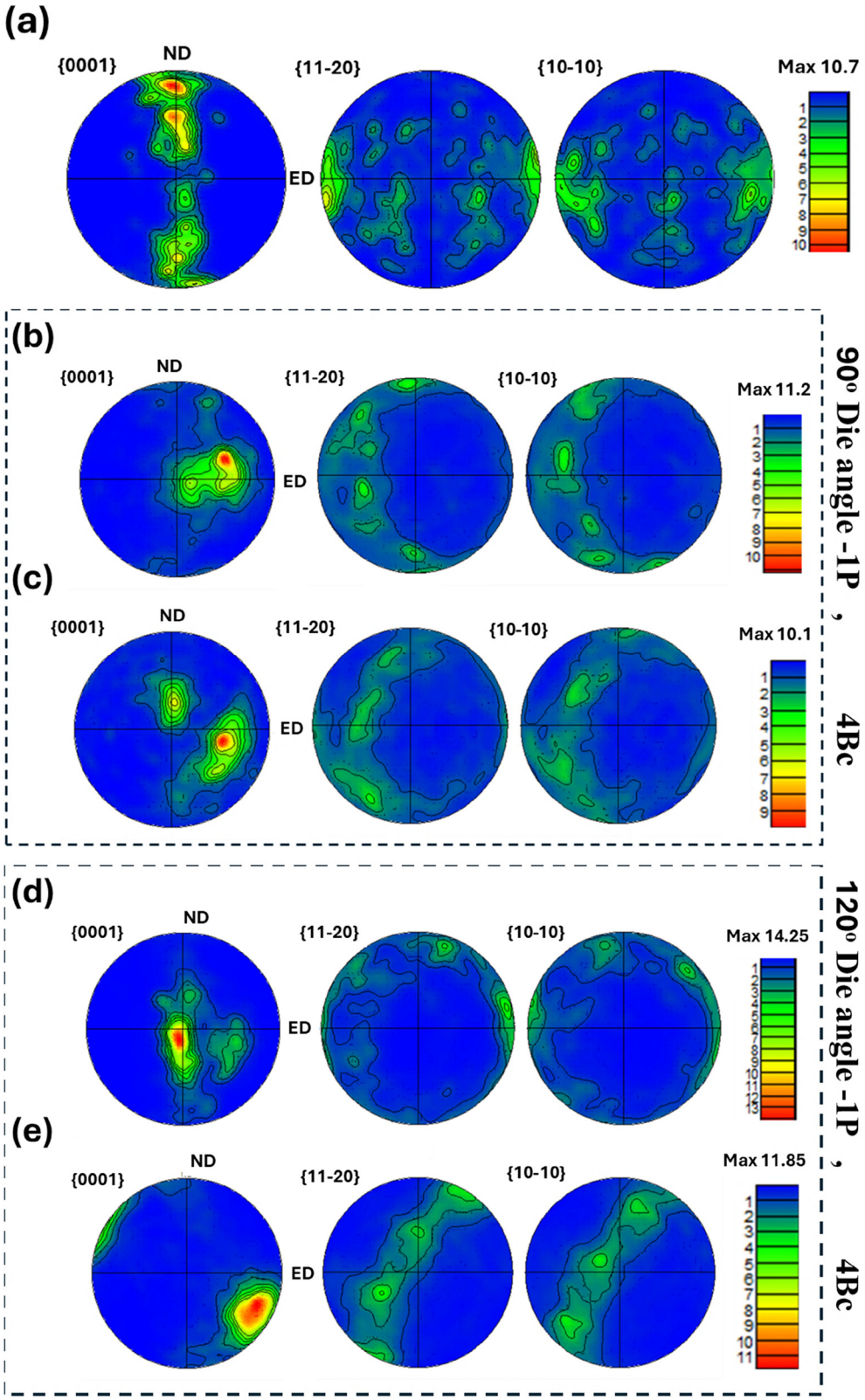

Figure 8: (0001), (11-20), (10-10) pole figures. EBSD data were acquired at 1 μm step size, and the color key is shown in the IPF map for (a) AA condition, (b) 1P_90° die, (c) 4Bc_90° die, (d) 1P_120° die, and (e) 4Bc_120° die.

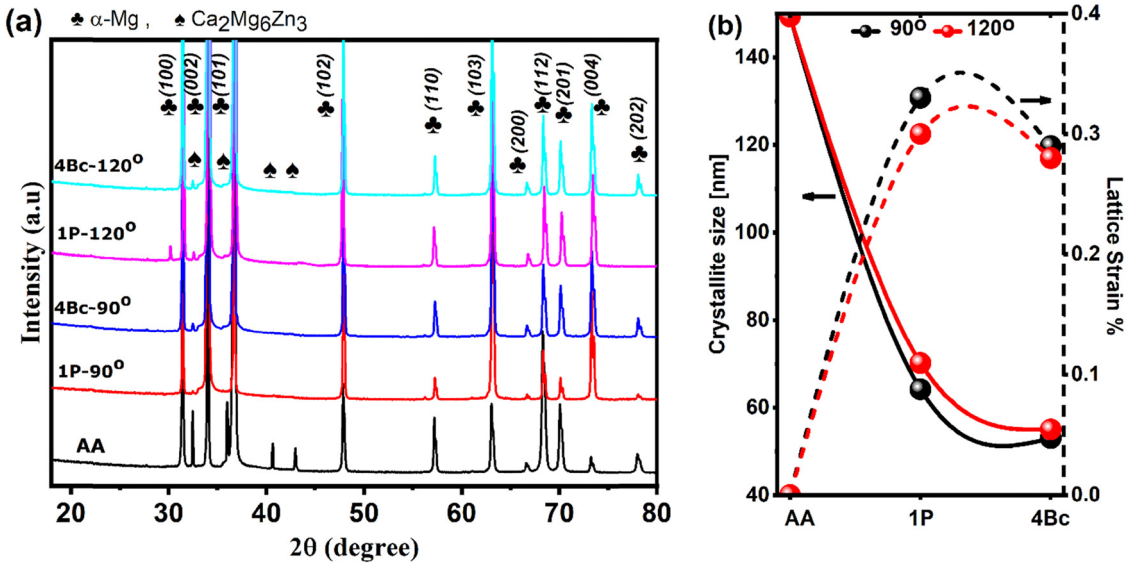

Figure 9: (a) XRD patterns of ZX30 AA and processed ECAP under different extrusion conditions and (b) evolution of crystallite size and lattice strain as a function of the number of passes for both dies.

shift in the XRD peaks, likely caused by the applied strain during ECAP, is observed. In the AA sample, the (100) and (101) planes exhibit strong intensities, but these diminish after a single ECAP pass for both die angles. Following four passes, the intensity of the (101) plane increases, while the (100) plane undergoes further reduction. These variations suggest modifications in texture and grain refinement, particularly as the shear deformation from ECAP progressively eliminated the pre-existing texture, allowing new textures to form with continued processing [57]. The (002) basal plane's orientation becomes more pronounced in ECAP-processed samples, aligning with the known behavior of Mg-alloys, where slip occurs more readily along compact planes like (002). The presence of intermetallic phases in the ZX30 alloy likely increases the stiffness of the (002) plane, promoting slip along other planes, such as (101). The increased intensity of the (002) peak in α-Mg-based materials after ECAP, as reported in previous studies, further supports these findings.

The Williamson-Hall analysis is employed to estimate crystallite size and micro-strain, considering uniform lattice strain in all crystallographic directions [58]. Peak broadening, influenced by crystallite size and strain, is accounted for by applying a crystallite shape factor (K = 0.9), X-ray wavelength (λ = 0.154 nm for Cu Kα radiation), and full width at half-maximum (β) of the diffraction peak (Figure 9b). The deformation imposed by the first ECAP pass significantly reduces the crystallite size to around 64 and 70 nm for the 90° and 120° dies, respectively, representing reductions of 57 and 53% compared to the AA sample. Concurrently, lattice strain increases significantly, consistent with observed microstructural changes.

After four passes (4Bc), no substantial changes in crystallite size or strain are noted, although processing fluctuations are observed. The 90° die imparts a more severe single-pass shear deformation than the 120° die, but the constant processing temperature played a crucial role in facilitating dynamic recrystallization and refining the microstructure. From a homogeneity perspective, larger die angles result in lower strain but require greater pressing force. In this context, steady die channel displacement, aided by temperature, enhances strain uniformity across the sample [59]. In addition, the increased crystallite size after four passes may be attributed to enhanced grain boundary mobility, driven by excessive plastic deformation from ECAP. As more passes are performed, the lattice strain reaches saturation due to the equilibrium between work hardening and dynamic recovery, stabilizing the microstructure.

3.4 Electrochemical and degradation performance

Figure 10 and Table 2 present the results of linear potentiodynamic polarization for the examined alloy before and after ECAP processing. The results indicate that the corrosion behavior of the alloy is significantly influenced by the die angle and number of passes among ECAP processing parameters.

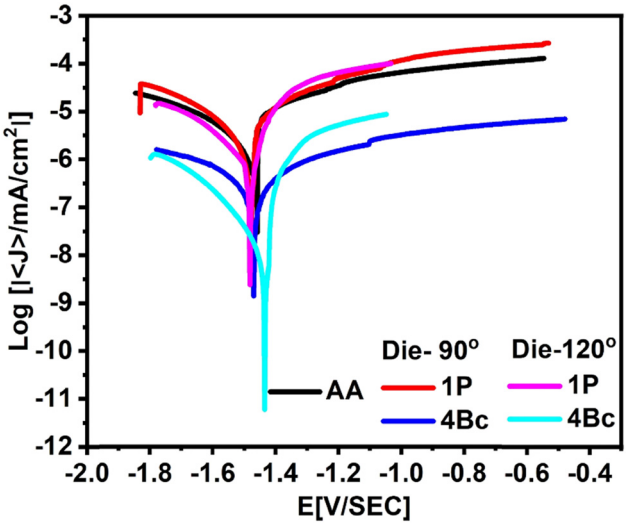

Figure 10: Linear potentiodynamic polarization curves of the AA and ECAPed billets of ZX30 alloy.

In the case of AA condition, the ZX30 alloy shows the highest corrosion rate of 0.15575 mmpy and a corrosion current density (i_{corr}) of 1.9626 × 10^{-6} A·cm^{-2} compared to the ECAP processed samples. This elevated rate can be attributed to the coarse grain structure, low grain boundary density, and microstructural heterogeneity, all of which facilitate corrosion initiation and propagation.

After one pass of ECAP processing with a 90° die angle, the alloy's corrosion rate and i_{corr} decreased by 70% each compared to the AA alloy, as listed in Table 2. This improvement is primarily due to grain refinement and increased dislocation density resulting from extensive plastic deformation during ECAP. The grain boundary area significantly increases, acting as a barrier to corrosion processes. Grain boundaries impede corrosion by restricting dislocation motion and reducing electrochemical activity at the grain surface. Increasing the ECAP passes up to 4Bc led to a steady decrease in the corrosion rate when compared to the 1P sample, with a reduction of 78% and 93% when compared to the AA condition, as presented in Table 2. This result indicates that the additional passes lead to further grain refinement, creating a highly homogenized, refined microstructure with remarkable improved corrosion resistance, in line with previous work [60].

Alternatively, when the die angle was set at 120° with one pass, the rate of corrosion reduced from 0.15576 to 0.06078 mmpy, showing a decrease in i_{corr} from 1.9626 × 10^{-6} to 7.2787 × 10^{-8} A·cm^{-2}, as compared to AA condition. In comparison to the 90° die, this pass generates less strain, which results in less grain refinement but still improves corrosion resistance when compared to the AA condition. An improvement in corrosion prevention is suggested by the E_{corr} shifting to −1.4207 V, a more noble value than the AA condition. The corrosion rate, i_{corr} at 1.0561 × 10^{-8} A·cm^{-2}, maintains the lowest value of 0.008926 mmpy after four sequential passes at a 120° die angle. Such observation denotes a significant improvement because sequential passes at a 120° die angle are still effective in grain refinement and microstructural homogeneity to a comparable level to that of the 90° die angle. Nonetheless, the increased die angle requires lesser strain per pass, as a result gradually refining the structure but in a uniform manner. The anodic region slopes beta (βa = 0.069417 V/dec) and the cathodic region slope minus beta c (−βc = 0.12075 V/dec) are less than what was experienced for the 90° die angle after four passes suggesting there are more even patterns of corrosion with less reaction kinetics in either the dissolution or hydrogen evolution reaction. Value of E_{corr} at −1.4602 V appears very close to that in the AA condition, demonstrates relatively stable conditions of the refined grains produced after four passes.

The potentiodynamic polarization curves provide insight into the kinetics of the corrosion process. As the grain size decreases, the corrosion current density (i_{corr}) decreases, reflecting a reduction in the overall corrosion activity. The finer the grain structure, the lower the corrosion rate, as seen in the four-pass samples for both 90° and 120° die angles.

The EIS plots shown in Figure 11 and data presented in Table 3 provide significant effects on the corrosion properties, especially charge transfer and capacitive behavior of ZX30 alloy with ECAP processing. The Nyquist plots of an

Table 2: Electrochemical parameters obtained from potentiodynamic polarization curves of ZX30 Mg billets before and after ECAP processing

Condition	βa (V/dec)	−βc (V/dec)	E_{corr} (V)	i_{corr} (A·cm^{-2})	Corrosion rate (mmpy)
AA	0.082772	0.22653	−1.4598	1.9626 × 10^{-6}	0.15576
1P_90°	0.026152	0.29864	−1.4806	5.8672 × 10^{-7}	0.046564
4Bc_90°	0.15377	0.12885	−1.4719	1.2819 × 10^{-7}	0.010174
1P_120°	0.087455	0.13823	−1.4207	7.2787 × 10^{-8}	0.06078
4Bc_120°	0.069417	0.12075	−1.4602	1.0561 × 10^{-8}	0.008926

AA alloy and the ECAP-processed one are shown in Figure 11a. It may be observed that the type of capacitive response at intermediate to high frequencies is common for all Mg alloys [51]. This capacitive semicircle comes from the resistance to charge transfer in alloying and double-layer capacitance [61,62]. The plots of the AA sample exhibited a small semicircle, whereas that for ECAPed ZX30 samples showed larger semicircles than those for their respective AA counterparts (Figure 11a) which correlated well with potentiodynamic polarization results, indicating that the corrosion reaction at ZX30 alloy/solution interface decreases with the decrease in grain size.

The Bode impedance plots of the AA and ECAP-processed ZX30 Mg alloys are presented in Figure 11b. At lower and moderate frequencies (up to 1.8 Hz), the impedance values significantly increase, with the ECAP-processed samples exhibiting higher values than the AA samples. Notably, in low-frequency ranges, higher impedance values suggest a more effective corrosion barrier [63]. The equivalent circuit model fitted to impedance spectra is presented in Figure 11a. The model comprises the following components: (Rs) representing the resistance of the solution, (Rp) denoting the electric charge transfer resistance at the phase boundary of the ZX30 alloy and the solution, as well as the charge transfer resistance through the double layer, and (CPE) refers to the constant phase element that characterizes the electrical properties of the double layer at the interface. The corresponding parameters fitted by the equivalent circuit are summarized in Table 3. It is well-known that higher Rp values represent less reactivity toward corrosion, so the AA sample presented a lower resistance to polarization (Rp = 232.8 Ω·cm^2), and on the other hand, samples ECAPed for four passes – mainly those in 4Bc-90° condition – exhibited very high Rp values up to 824.4 Ohm·cm^2. This reflects the significantly enhanced charge transfer resistance, correlating with the refined microstructure that inhibits corrosion propagation. As the CPE values are indicative of capacitive behavior, with the 4Bc samples showing lower CPE values (*e.g.*, 5.6815 × 10^{-6} F for 4Bc-90°), suggesting a more stable and protective oxide layer formed on the surface. In the Bode plots shown in Figure 11b, indicating phase angles show more capacitive response in ECAP samples against AA confirmation that grain refinement by ECAP reduce active area to be corroded. EIS results are in good agreement with that obtained through linear polarization data, showing a considerable enhancement of corrosion resistance from grain boundaries enrichment and homogenized/finer microstructure owing to ECAP processing. Higher Rp values and lower capacitance in the ECAPed samples insinuate reduced electrochemical activity, which agrees with a more stable protective film formation that coincides well with the lower corrosion rates/currents observed from the polarization data.

Table 3: Electrical parameters of the EIS equivalent circuit

Condition	Rs (Ω·cm^2)	Rp (Ω.cm^2)	CPE (F)	*N*
AA	55.3	232.8	4.8623 × 10^{-6}	0.84
1P_90°	38.2	465.5	9.2171 × 10^{-6}	0.96
4Bc_90°	48.6	824.4	5.6815 × 10^{-6}	0.80
1P_120°	65.5	436	4.84 × 10^{-6}	0. 84
4Bc_120°	68.8	808	6.28 × 10^{-6}	0.81824

For further investigation, the weight loss test was conducted in Ringer lactate for up to 15 days which is meant to

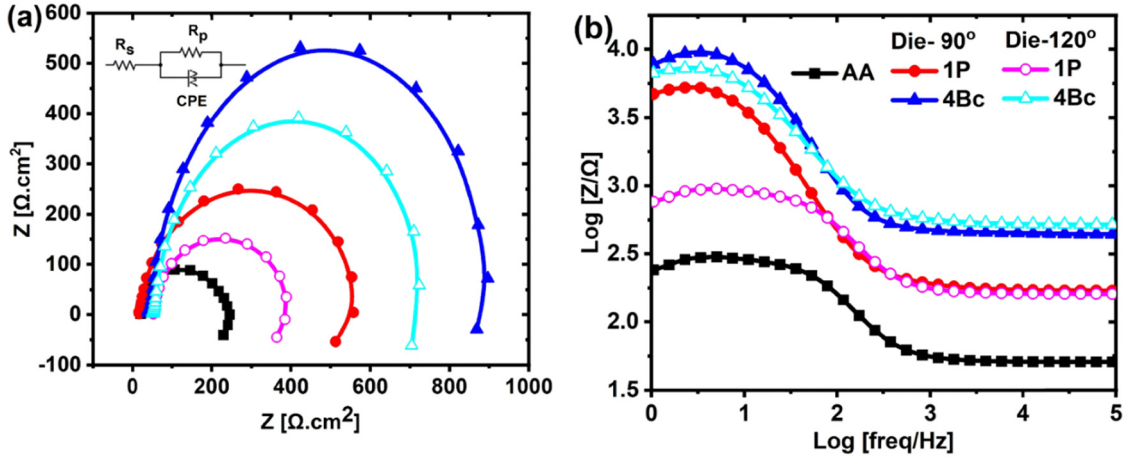

Figure 11: EIS diagrams: (a) Nyquist plot coupled with the equivalent circuit and (b) Bode plot with phase angles of the AA and ECAPed billets of ZX30 alloy.

give important insights into how the ECAP processing affects the corrosion resistance of ZX30 alloy. The results of the weight loss test are presented in Figure 12. By comparing the trends between weight loss and linear potentiodynamic polarization methods, more meaningful conclusions were made concerning the interaction of grain size, parameters of the ECAP processing, and corrosion behavior. In the AA condition, the samples exhibit the highest weight loss, reaching 14 mg after 360 h, which suggests a significant degradation due to the coarse grain structure and low grain boundaries that promote faster corrosion. The lack of substantial grain refinement exposes the surface to corrosive attack leading to gradual corrosion of the material over a period.

On the other hand, samples subjected to ECAP processing show a significant improvement in corrosion resistance and have decreased losses with increasing number of passes. At 1P- 90° die angle, there is remarkable weight loss decrease of 4.6 mg, suggesting that there is grain structure enhancement at this moment improving corrosion resistance. The finer grains and the higher density of grain boundaries enhanced slow-down of the rate of corrosion since these acted as barriers to the diffusion of the corrosive agents. After 4Bc-90°, the weight loss further drops to 3 mg, this indicates increased protection from more refined and homogenized microstructures. Such a well refined grain structure created a more stable and homogenous surface, which helped in reducing localized corrosion and the rate of deterioration over time. Also, the samples with a 120° die angle have positive changes with the weight loss correcting itself to approximately 5.3 mg after one pass (1P-120°) and it reduces further to 2.55 mg after four passes (4Bc-120°). It can be summarized that both 90° and 120° die configurations are better, as with the increase in number of passes, corrosion resistance improves primarily due to the grain size and microstructure homogeneity. Finer grains and the increased grain boundary density act as effective barriers against corrosion, slowing the rate of material degradation, as reflected by the lower weight loss in these conditions. The refined microstructure produced by ECAP, especially after four passes, offers superior protection against corrosion in corrosion environments, and further assistance for the alloys making them suitable for biomedical applications where corrosion protection is critical.

The weight loss results support the data concerning linear polarized corrosion values, where the weight loss and the current density decreased with the increase in passes and decrease in die angle. These findings confirm that the increase in level of grain refinement *via* ECAP increases the corrosion resistance of the samples since fine grained structures decrease the electro-active and electrochemically susceptible surface areas.

Overall, ECAP processing significantly enhances the corrosion resistance of the ZX30 Mg alloy; the primary factors influencing this improvement are the die angle and the number of passes applied during processing. These findings suggest that alloys processed through ECAP could be suitable, for applications that demand improved resistance against corrosion, such as in implants and various components in the sector which show a growing interest in utilizing Mg alloys.

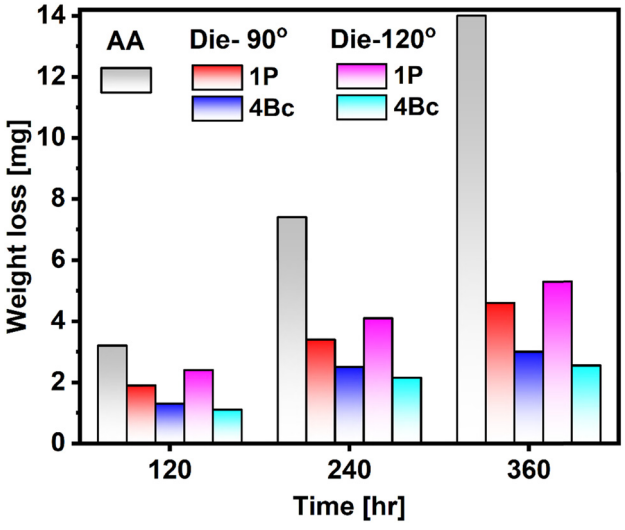

Figure 12: Mass loss of ZX30 alloy immersed in ringer's lactate electrolyte before and after ECAP processing.

3.5 Mechanical behavior

The tensile and hardness results for the AA and ECAP-processed samples using the Bc route are presented in Figure 13. It is clear from Figure 13a that both the processing route and the number of passes directly influence the yield strength (σ_y), ultimate tensile strength (σ_u), and elongation to failure (E_F%). The AA sample exhibits lower σ_y and σ_u due to its coarse-grained microstructure and the presence of secondary phases along grain boundaries. After ECAP processing, the mechanical properties improve as a result of the dissolution of secondary phases [64]. As the number of passes increases, both σ_y and σ_u increase, while E_F% decreases. However, the die angle has a notable effect on these mechanical properties, as seen in Figure 13b and c. For the one pass process, the highest values for σ_y and σ_u are obtained with a 90° die angle, both exhibiting enhancements of approximately 32% compared to the AA condition. However, this improvement is

accompanied by a decrease in E_F%, which dropped by about 20 and 9% relative to the AA and 1P-120° conditions, respectively. Interestingly, this trend reverses under the 4-pass condition (4Bc), where the 120° die angle yields the greatest improvement in mechanical strength. After the 4Bc *via* the 120° die angle, σ_u reaches its maximum, showing a 56 and 26% enhancement compared to the AA and 1P-120° conditions, respectively. Notably, no significant difference is observed between the 4Bc-120° and 4Bc-90° die angles, confirming the 4Bc route as the optimal processing condition for maximizing strength while balancing grain refinement and strain hardening, and avoiding excessive recovery. In the one pass condition, dislocation multiplication raises dislocation density, impeding further motion and strengthens the material. With additional passes, there is a substantial increase in dislocation boundaries, leading to subgrains formation of and a refined grain structure, consistent with the Hall–Petch relationship [65,66]. As illustrated in Figure 13b and c, significant grain size reduction is accompanied by mechanical improvements. The transition from LABs to HABs further enhances strength by restricting dislocation movement.

Vickers' hardness results for the AA and ECAP-processed ZX30 alloy, as shown in Figure 13b and c, reveal that increasing the number of ECAP passes consistently improves hardness. The highest hardness value, 92 HV, is achieved with the 4Bc-120° die angle, representing increases of 66 and 58% compared to the AA and 4Bc-90° conditions, respectively. These mechanical results correspond well with the observed grain refinement, texture modification, and strain accumulation during ECAP. The

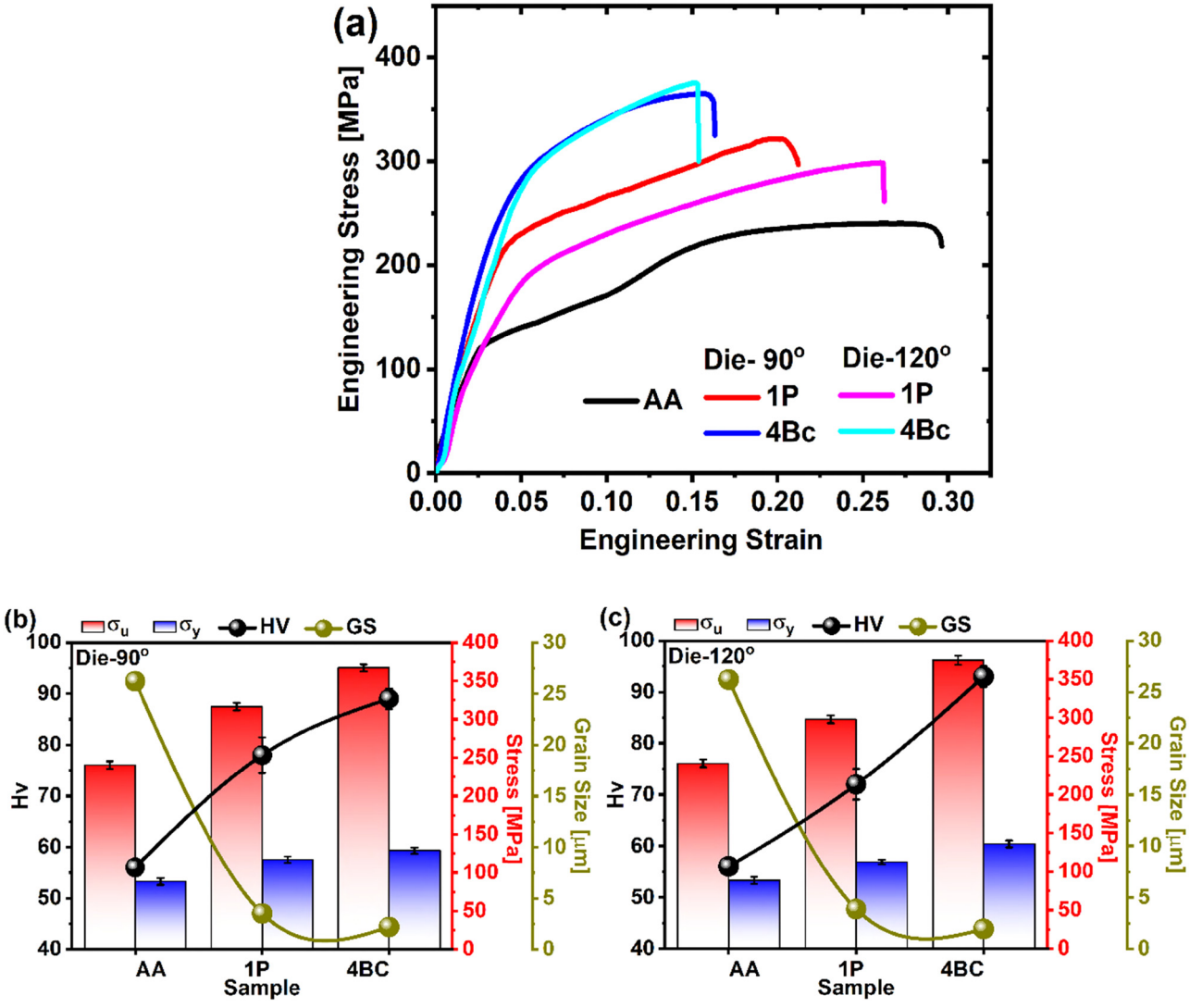

Figure 13: (a) Engineering stress-strain results from tensile tests of ZX30 samples processed under different conditions. (b) Hardness results and extracted mechanical properties from (a), including grain size, for samples processed with a 90° die angle, and (c) for a 120° die angle.

interplay between slip system activation and twinning also influences texture formation, which subsequently affects mechanical properties. The reduction in ductility following ECAP processing is attributed to the crystal structure, which plays an important role in dictating the mechanical properties. However, in all studied conditions, elongation to failure remains above 15%, reaching up to 26%. Figure 13a shows that the highest strength is achieved after four Bc passes, while maintaining 26% ductility. This indicates that although there is a classic tradeoff between strength and ductility, increasing the number of passes allows for a balanced improvement in both. A possible explanation for the moderate ductility observed after four passes is the homogeneous distribution of fine grains. This combination of high strength and moderate ductility due to bimodal grain size distributions has been reported in previous studies [67]. Furthermore, prior studies suggest that the variation in elongation may reflect differences in microstructure anisotropy. An isotropic microstructure promotes uniform deformation and higher elongation, while an anisotropic microstructure with elongated HABs may lead to early crack formation and reduced elongation to failure [68].

4 Conclusion

This study investigates the evolution of microstructure, texture, electrochemical properties, and mechanical performance in ZX30 alloy processed by ECAP under varying pass numbers and die angles. Key findings are summarized as follows:

1) The ECAP process achieves substantial grain refinement, with dynamic recrystallization reducing grain size from 26.2 μm in the AA alloy to 2.2 and 1.9 μm after 4Bc for 90° and 120° die angles, respectively.
2) XRD analysis shows diffraction peaks mainly indexed to the α-Mg phase, with secondary $Ca_2Mg_6Zn_3$ phases comprising approximately 3.5% of the alloy volume. After ECAP, these phases dispersed and dissolved within the Mg matrix, improving microstructural homogeneity.
3) The ECAP leads to peak broadening due to crystallite size reduction and increased lattice strain, with initial crystallite sizes decreasing by 57% (~64 nm) and 53% (~70 nm) for the 90° and 120° dies, respectively, after one pass.
4) Processing through 4Bc using the 90° die and 120° die results in a reduction of the corrosion rate by 93.4 and 94.2%, respectively compared to the AA condition.
5) The 4Bc process using the 90° and 120° dies shows significant improvement in the polarization resistance, increasing by 254 and 247%, respectively compared to the AA condition.
6) A 15-day immersion test in Ringer lactate solution demonstrates improved corrosion resistance in ECAP-processed samples. The AA condition exhibits the highest weight loss (14 mg after 360 h), while the 4Bc samples exhibit reduced losses of 3 mg and 2.55 mg for the 90° and 120° dies, respectively, corroborating the linear polarization results.
7) Ultimate tensile strength increases from 240 MPa in the AA alloy to 367 and 375.6 MPa after 4Bc for the 90° and 120° dies, respectively.
8) Hardness values rise from 56 Hv in the AA condition to 89 Hv and 93 Hv after 4Bc for the 90° and 120° die angles, respectively.

Acknowledgments: The researchers would like to thank the Deanship of Graduates Studies and Scientific Research at Qassim University for financial support (QU-APC-2025).

Funding information: The financial support from the Deanship of Graduates Studies and Scientific Research at Qassim University (QUAPC-2025).

Author contributions: Abdulrahman I. Alateyah: project administration, conceptualization, validation, and project supervision. Adel M. A. Mohamed: formal analysis, investigation, and writing – original draft. Waleed H. El-Garaihy: project administration, conceptualization, methodology, investigation, and writing – review and editing. Majed Alinizzi: data curation, validation, and formal analysis. Mansour Alturki: investigation and formal analysis. Mohamed S. El-Asfoury: methodology, investigation, and writing – original draft. Eman Zayed: methodology and visualization. Hussein Zein: methodology and data curation. All authors have accepted responsibility for the entire content of this manuscript and approved its submission.

Conflict of interest: The authors state no conflict of interest.

Data availability statement: The datasets generated and/or analyzed during the current study are available from the corresponding author on reasonable request.

References

[1] Atrens, A., G.-L. Song, M. Liu, Z. Shi, F. Cao, and M. S. Dargusch. Review of recent developments in the field of magnesium corrosion. *Advanced Engineering Materials*, Vol. 17, 2015, pp. 400–453.

[2] Luo, A. A. Magnesium casting technology for structural applications. *Journal of Magnesium and Alloys*, Vol. 1, 2013, pp. 2–22.
[3] Wang, J., Z. Wan, J. Wang, Y. Zou, J. Xu, J. Wang, et al. The research progress of magnesium alloy building formwork. *Materials*, Vol. 17, 2024, id. 3570.
[4] Atrens, A., G.-L. Song, F. Cao, Z. Shi, and P. K. Bowen. Advances in Mg corrosion and research suggestions. *Journal of Magnesium and Alloys*, Vol. 1, 2013, pp. 177–200.
[5] Lin, X., L. Tan, Q. Zhang, K. Yang, Z. Hu, J. Qiu, et al. The in vitro degradation process and biocompatibility of a ZK60 magnesium alloy with a forsterite-containing micro-arc oxidation coating. *Acta Biomaterialia*, Vol. 9, 2013, pp. 8631–8642.
[6] Wang, D., Y. Wang, J. Wang, K. Ma, C. Dai, J. Wang, et al. Corrosion resistance of Mg-Al-Zn magnesium alloy concrete formwork in Portland cement paste. *Construction and Building Materials*, Vol. 325, 2022, id. 126745.
[7] Zeng, R., W. Dietzel, F. Witte, N. Hort, and C. Blawert. Progress and challenge for magnesium alloys as biomaterials. *Advanced Engineering Materials*, Vol. 10, 2008, pp. B3–B14.
[8] Jin, Z.-Z., M. Zha, S.-Q. Wang, S.-C. Wang, C. Wang, H.-L. Jia, et al. Alloying design and microstructural control strategies towards developing Mg alloys with enhanced ductility. *Journal of Magnesium and Alloys*, Vol. 10, 2022, pp. 1191–1206.
[9] Witte, F., V. Kaese, H. Haferkamp, E. Switzer, A. Meyer-Lindenberg, C. J. Wirth, et al. In vivo corrosion of four magnesium alloys and the associated bone response. *Biomaterials*, Vol. 26, 2005, pp. 3557–3563.
[10] Hornberger, H., S. Virtanen, and A. R. Boccaccini. Biomedical coatings on magnesium alloys – A review. *Acta Biomaterialia*, Vol. 8, 2012, pp. 2442–2455.
[11] Chen, X. B., N. Birbilis, and T. B. Abbott. Review of corrosion-resistant conversion coatings for magnesium and its alloys. *Corrosion*, Vol. 67, 2011, id. 035005-1-035005–16.
[12] Ratna Sunil, B., T. S. Sampath Kumar, U. Chakkingal, V. Nandakumar, and M. Doble. Friction stir processing of magnesium–nanohydroxyapatite composites with controlled in vitro degradation behavior. *Materials Science and Engineering: C*, Vol. 39, 2014, pp. 315–324.
[13] Uppal, G., A. Thakur, A. Chauhan, and S. Bala. Magnesium based implants for functional bone tissue regeneration – A review. *Journal of Magnesium and Alloys*, Vol. 10, 2022, pp. 356–386.
[14] Chen, J., Y. Xu, S. K. Kolawole, J. Wang, X. Su, L. Tan, et al. Systems, properties, surface modification and applications of biodegradable magnesium-based alloys: A review. *Materials*, Vol. 15, 2022, id. 5031.
[15] Dziuba, D., A. Meyer-Lindenberg, J. M. Seitz, H. Waizy, N. Angrisani, and J. Reifenrath. Long-term in vivo degradation behaviour and biocompatibility of the magnesium alloy ZEK100 for use as a biodegradable bone implant. *Acta Biomaterialia*, Vol. 9, 2013, pp. 8548–8560.
[16] El-Sanabary, S., H. Kouta, M. Shaban, A. Alrumayh, A. I. Alateyah, F. N. Alsunaydih, et al. A comparative study of machine learning and response surface methodologies for optimizing wear parameters of ECAP-processed ZX30 alloy. *Heliyon*, Vol. 10, 2024, id. e33967.
[17] Hrapkowicz, B., S. Lesz, M. Karolus, D. Garbiec, J. Wiśniewski, R. Rubach, et al. Microstructure and Mechanical Properties of Spark Plasma Sintered Mg-Zn-Ca-Pr Alloy. *Metals (Basel)*, Vol. 12, 2022, id. 375.
[18] Li, N. and Y. Zheng. Novel magnesium alloys developed for biomedical application: A review. *Journal of Materials Science & Technology*, Vol. 29, 2013, pp. 489–502.
[19] Xu, L., X. Liu, K. Sun, R. Fu, and G. Wang. Corrosion behavior in magnesium-based alloys for biomedical applications. *Materials*, Vol. 15, 2022, id. 2613.
[20] Salahshoor, M. and Y. B. Guo. Surface integrity of biodegradable Magnesium–Calcium orthopedic implant by burnishing. *Journal of the Mechanical Behavior of Biomedical Materials*, Vol. 4, 2011, pp. 1888–1904.
[21] Ilich, J. Z. and J. E. Kerstetter. Nutrition in bone health revisited: A story beyond calcium. *Journal of the American College of Nutrition*, Vol. 19, 2000, pp. 715–737.
[22] Sun, Y., B. Zhang, Y. Wang, L. Geng, and X. Jiao. Preparation and characterization of a new biomedical Mg–Zn–Ca alloy. *Materials & Design*, Vol. 34, 2012, pp. 58–64.
[23] Alateyah, A. I., A. BaQais, M. M. Z. Ahmed, Y. Zedan, M. O. Alawad, M. S. El-Asfoury, et al. Improved corrosion resistance and mechanical properties of severely deformed ZM31 alloy. *Heliyon*, Vol. 10, 2024, id. e26400.
[24] Argade, G. R., K. Kandasamy, S. K. Panigrahi, and R. S. Mishra. Corrosion behavior of a friction stir processed rare-earth added magnesium alloy. *Corrosion Science*, Vol. 58, 2012, pp. 321–326.
[25] Hamu, G. B., D. Eliezer, and L. Wagner. The relation between severe plastic deformation microstructure and corrosion behavior of AZ31 magnesium alloy. *Journal of Alloys and Compounds*, Vol. 468, 2009, pp. 222–229.
[26] Wang, H., Y. Estrin, H. Fu, G. Song, and Z. Zúberová. The effect of pre-processing and grain structure on the bio-corrosion and fatigue resistance of magnesium alloy AZ31. *Advanced Engineering Materials*, Vol. 9, 2007, pp. 967–972.
[27] Bahmani, A., S. Arthanari, and K. S. Shin. Formulation of corrosion rate of magnesium alloys using microstructural parameters. *Journal of Magnesium and Alloys*, Vol. 8, 2020, pp. 134–149.
[28] Jafari, S., S. E. Harandi, and R. K. Singh Raman. A review of stress-corrosion cracking and corrosion fatigue of magnesium alloys for biodegradable implant applications. *JOM*, Vol. 67, 2015, pp. 1143–1153.
[29] Hofstetter, J., M. Becker, E. Martinelli, A. M. Weinberg, B. Mingler, H. Kilian, et al. High-strength low-alloy (HSLA) Mg–Zn–Ca alloys with excellent biodegradation performance. *JOM*, Vol. 66, 2014, pp. 566–572.
[30] El-Garaihy, W. H., A. I. Alateyah, M. M. Z. Ahmed, M. S. El-Asfoury, M. O. Alawad, A. BaQais, et al. Improving in-vitro corrosion and degradation performance of Mg–Zn–Ca alloy for biomedical applications by equal channel angular pressing. *Metals And Materials International*, Vol. 30, 2024, pp. 1701–1721.
[31] Ahmadkhaniha, D., Y. Huang, M. Jaskari, A. Järvenpää, M. H. Sohi, C. Zanella, et al. Effect of high-pressure torsion on microstructure, mechanical properties and corrosion resistance of cast pure Mg. *Journal of Materials Science*, Vol. 53, 2018, pp. 16585–16597.
[32] Pérez-Prado, M. T., D. Valle, and O. A. Ruano. Grain refinement of Mg–Al–Zn alloys via accumulative roll bonding. *Scripta Materialia*, Vol. 51, 2004, pp. 1093–1097.
[33] Nikfahm, A., I. Danaee, A. Ashrafi, and M. R. Toroghinejad. Corrosion behavior of ultra fine grain copper produced by accumulative roll bonding process. *Transactions of the Indian Institute of Metals*, Vol. 67, 2014, pp. 115–121.
[34] Alateyah, A. I., A. Alrumayh, O. alhabib, S. K. AlSulaim, M. A. S. Aljouie, M. Alqatuimy, et al. Effect of microstructural and texture evolution of ECAP-processed Mg-Zn-Zr alloy on the corrosion and wear behaviours for bone repair applications. *Journal of Engineering Research*, Vol. 13, 2025, pp. 445–452.

[35] Zhang, C. Z., S. J. Zhu, L. G. Wang, R. M. Guo, G. C. Yue, and S. K. Guan. Microstructures and degradation mechanism in simulated body fluid of biomedical Mg–Zn–Ca alloy processed by high pressure torsion. *Materials & Design*, Vol. 96, 2016, pp. 54–62.

[36] Chen, J., G. Chen, H. Yan, B. Su, X. Gong, and B. Zhou. Correlation between microstructure and corrosion resistance of magnesium alloys prepared by high strain rate rolling. *Journal of Materials Engineering and Performance*, Vol. 26, 2017, pp. 4748–4759.

[37] Song, D., A. B. Ma, J. H. Jiang, P. H. Lin, D. H. Yang, and J. F. Fan. Corrosion behaviour of bulk ultra-fine grained AZ91D magnesium alloy fabricated by equal-channel angular pressing. *Corrosion Science*, Vol. 53, 2011, pp. 362–373.

[38] Elkatatny, S., M. F. Alsharekh, A. I. Alateyah, S. El-Sanabary, A. Nassef, M. Kamel, et al. Optimizing the powder metallurgy parameters to enhance the mechanical properties of Al-4Cu/xAl_2O_3 composites using machine learning and response surface approaches. *Applied Sciences*, Vol. 13, 2023, id. 7483.

[39] Ralston, K. D., N. Birbilis, and C. H. J. Davies. Revealing the relationship between grain size and corrosion rate of metals. *Scripta Materialia*, Vol. 63, 2010, pp. 1201–1204.

[40] Ralston, K. D., D. Fabijanic, and N. Birbilis. Effect of grain size on corrosion of high purity aluminium. *Electrochimica Acta*, Vol. 56, 2011, pp. 1729–1736.

[41] Zhu, S. Q., H. G. Yan, J. H. Chen, Y. Z. Wu, B. Su, Y. G. Du, et al. Feasibility of high strain-rate rolling of a magnesium alloy across a wide temperature range. *Scripta Materialia*, Vol. 67, 2012, pp. 404–407.

[42] Prithivirajan, S., G. M. Naik, S. Narendranath, and V. Desai. Recent progress in equal channel angular pressing of magnesium alloys starting from Segal's idea to advancements till date – A review. *International Journal of Lightweight Materials and Manufacture*, Vol. 6, 2023, pp. 82–107.

[43] Krajňák, T., P. Minárik, J. Stráská, J. Gubicza, K. Máthis, and M. Janeček. Influence of equal channel angular pressing temperature on texture, microstructure and mechanical properties of extruded AX41 magnesium. *Journal of Alloys and Compounds*, Vol. 705, 2017, pp. 273–282.

[44] Shaban, M., M. F. Alsharekh, F. N. Alsunaydih, A. I. Alateyah, M. O. Alawad, A. BaQais, et al. Investigation of the effect of ECAP parameters on hardness, tensile properties, impact toughness, and electrical conductivity of pure Cu through machine learning predictive models. *Materials*, Vol. 15, 2022, id. 9032.

[45] Biswas, S., S. Singh Dhinwal, and S. Suwas. Room-temperature equal channel angular extrusion of pure magnesium. *Acta Materialia*, Vol. 58, 2010, pp. 3247–3261.

[46] King, A. D., N. Birbilis, and J. R. Scully. Accurate electrochemical measurement of magnesium corrosion rates; a combined impedance, mass-loss and hydrogen collection study. *Electrochimica Acta*, Vol. 121, 2014, pp. 394–406.

[47] El-Garaihy, W. H., A. I. Alateyah, M. O. Alawad, F. N. Alsunaydih, S. El-Sanabary, M. S. El-Asfoury, et al. Optimization of ECAP parameters of ZX30 alloy using feature engineering assisted machine learning and response surface approaches. *Materials Today Communications*, Vol. 40, 2024, id. 109560.

[48] Shaban, M., F. N. Alsunaydih, H. Kouta, S. El-Sanabary, A. Alrumayh, A. I. Alateyah, et al. Optimization of wear parameters for ECAP-processed ZK30 alloy using response surface and machine learning approaches: A comparative study. *Scientific Reports*, Vol. 14, 2024, id. 9233.

[49] Yang, C.-M., Y.-H. Chen, M.-H. Tsai, B. B.-Y. Hsu, W.-T. Tsai, C.-F. Lin, et al. Observation of morphology and compositional changes of magnesium alloy using liquid cell TEM. *Journal of Materials Research and Technology*, Vol. 21, 2022, pp. 4548–4557.

[50] Liu, C., X. Chen, J. Chen, A. Atrens, and F. Pan. The effects of Ca and Mn on the microstructure, texture and mechanical properties of Mg-4 Zn alloy. *Journal of Magnesium and Alloys*, Vol. 9, 2021, pp. 1084–1097.

[51] Prithivirajan, S., S. Narendranath, and V. Desai. Analysing the combined effect of crystallographic orientation and grain refinement on mechanical properties and corrosion behaviour of ECAPed ZE41 Mg alloy. *Journal of Magnesium and Alloys*, Vol. 8, 2020, pp. 1128–1143.

[52] Sahoo, P. S., M. M. Mahapatra, P. R. Vundavilli, R. K. Sabat, S. Sirohi, and S. Kumar. Investigation of severe plastic deformation effects on magnesium RZ5 alloy sheets using a modified multi-pass equal channel angular pressing (ECAP) technique. *Materials*, Vol. 16, 2023, id. 5158.

[53] Galiyev, A., R. Kaibyshev, and G. Gottstein. Correlation of plastic deformation and dynamic recrystallization in magnesium alloy ZK60. *Acta Materialia*, Vol. 49, 2001, pp. 1199–1207.

[54] Figueiredo, R. B. and T. G. Langdon. Grain refinement and mechanical behavior of a magnesium alloy processed by ECAP. *Journal of Materials Science*, Vol. 45, 2010, pp. 4827–4836.

[55] Ma, Y., F.-Y. Han, C. Liu, and M.-Z. Li. Microstructure, texture evolution, and mechanical properties of ECAP-processed ZAT522 magnesium alloy. *Acta Metallurgica Sinica (English Letters)*, Vol. 33, 2020, pp. 233–242.

[56] Moreno, L., E. Matykina, K. A. Yasakau, C. Blawert, R. Arrabal, and M. Mohedano. As-cast and extruded Mg Zn Ca systems for biodegradable implants: Characterization and corrosion behavior. *Journal of Magnesium and Alloys*, Vol. 11, 2023, pp. 1102–1120.

[57] Feng, X. and T. AI. Microstructure evolution and mechanical behavior of AZ31 Mg alloy processed by equal-channel angular pressing. *Transactions of Nonferrous Metals Society of China*, Vol. 19, 2009, pp. 293–298.

[58] Mote, V., Y. Purushotham, and B. Dole. Williamson-Hall analysis in estimation of lattice strain in nanometer-sized ZnO particles. *Journal of Theoretical and Applied Physics*, Vol. 6, 2012, id. 6.

[59] Awang Sh'ri, D. N., Z. S. Zahari, and A. Yamamoto. Effect of ECAP die angle on mechanical properties and biocompatibility of SS316L. *Metals (Basel)*, Vol. 11, 2021, id. 1513.

[60] Alateyah, A. I., T. A. Aljohani, M. O. Alawad, H. A. El-Hafez, A. N. Almutairi, E. S. Alharbi, et al. Improved corrosion behavior of AZ31 alloy through ECAP processing. *Metals (Basel)*, Vol. 11, 2021, id. 363.

[61] Sadawy, M. M. and M. Ghanem. Grain refinement of bronze alloy by equal-channel angular pressing (ECAP) and its effect on corrosion behaviour. *Defence Technology*, Vol. 12, 2016, pp. 316–323.

[62] Alateyah, A. I., M. M. Z. Ahmed, M. M. E.-S. Seleman, S. Elkatatny, M. Alturki, A. Nassef, et al. Characterization of microstructure, crystallographic texture, corrosion behavior and mechanical properties of severely deformed AA7075 alloy. *Results in Engineering*, Vol. 25, 2025, id. 103749.

[63] Gu, Y., A. Ma, J. Jiang, H. Li, D. Song, H. Wu, et al. Simultaneously improving mechanical properties and corrosion resistance of pure Ti by continuous ECAP plus short-duration annealing. *Materials Characterization*, Vol. 138, 2018, pp. 38–47.

[64] Naik, G. M., S. Narendranath, and S. S. S. Kumar. Effect of ECAP die angles on microstructure mechanical properties and corrosion behavior of AZ80 Mg alloy. *Journal of Materials Engineering and Performance*, Vol. 28, 2019, pp. 2610–2619.

[65] Sadi, S., A. Hanna, T. Baudin, F. Brisset, J. M. Cabrera, and H. Azzeddine. Microstructure and texture evolution of ECAP-processed Mg-Ce alloy during isothermal annealing. *Materials Today Communications*, Vol. 32, 2022, id. 103920.

[66] Alateyah, A. I., M. Alinizzi, H. Zein, H. Kouta, M. Shaban, M. O. Alawad, et al. Optimizing wear behavior of AA7075 processed via ECAP: An integrated experimental, computational, and machine learning approach. *Materials Today Communications*, Vol. 47, 2025, id. 113075.

[67] Manjunath Naik, G., S. Bandadka, M. Mallaiah, R. Ishwar Badiger, and N. Sannayellappa. Effect of ECAE die angle on microstructure mechanical properties and corrosion behavior of AZ80/91 magnesium alloys. *Magnesium Alloys Structure and Properties*, IntechOpen, London, 2022.

[68] Zhao, X., X. Yang, X. Liu, C. T. Wang, Y. Huang, and T. G. Langdon. Processing of commercial purity titanium by ECAP using a 90 degrees die at room temperature. *Materials Science and Engineering: A*, Vol. 607, 2014, pp. 482–489.